Heat transfer and flow structure in annular convection

Yuejia Zhang
NYU-ECNU Institute of Physics and Institute of Mathematical Sciences, New York University Shanghai, Shanghai, 200124, China

Nicholas J. Moore*
Department of Mathematics, Colgate University, Hamilton, NY 13346, USA

Jinzi Mac Huang†
NYU-ECNU Institute of Physics and Institute of Mathematical Sciences, New York University Shanghai, Shanghai, 200124, China and
Applied Math Lab, Courant Institute, New York University, New York, NY 10012, USA

(Dated: November 25, 2024)

The heat transfer of fluid can be greatly enhanced by natural convection, leading to the famous Nusselt-Rayleigh number scaling that has been a focus of modern fluid dynamics. Our work explores natural convection in an annular domain, where the annular geometry reinforces the large-scale circulation and leads to an altered Nusselt-Rayleigh number scaling. To understand the heat transfer and flow pattern in this novel geometry, we derive a reduced model from the Navier-Stokes-Boussinesq equations where the equations of flow and heat are transformed to a system of low-order partial differential equations, whose solution preserves the same boundary layer structures seen in the direct numerical simulation. By matching the solutions inside and outside the boundary layer, we recover all the scaling laws observed in the direct numerical simulation, further demonstrating the accuracy of this reduced model. Our results also provide a systematic way of analyzing thermal convection in an annular domain, which brings us one step closer to understanding the origin of large-scale circulation and the mechanism of convective heat transfer.

I. INTRODUCTION

Buoyancy variations resulting from the uneven heating of a fluid create a complex motion known as thermal convection. On a planetary scale, thermal convection brings motion to an otherwise motionless world, leading to atmospheric and oceanic flows [1, 2], mantle and liquid-core convection [3–7], solar magneto-hydrodynamics [8], and more.

As a relative measure between the buoyancy and viscous forcing, the Rayleigh number Ra dictates the dynamics of thermal convection: Below a critical number $\mathrm{Ra} < \mathrm{Ra}_1^*$, viscosity damps any motion and the fluid conducts heat as a solid would; At high Ra, convective motion becomes turbulent, leading to dynamical features such as a large-scale circulation (LSC) and enhanced heat transfer [9].

Dimensionlessly, heat transfer is characterized by the Nusselt number, which is the ratio of convective to conductive heat transfer. For $\mathrm{Ra} \leq \mathrm{Ra}_1^*$, heat transfer is purely conductive, giving $\mathrm{Nu} = 1$. For $\mathrm{Ra} \gg \mathrm{Ra}_1^*$, vigorous convective motion enhances the heat transfer considerably, and a power-law relationship $\mathrm{Nu} \propto \mathrm{Ra}^{\beta}$ has been observed in the range from $\mathrm{Ra} = 10^6$ to $\mathrm{Ra} = 10^{14}$ [10, 11]. The classical scaling of $\beta = 1/3$ can be shown from the boundary layer analysis [12, 13]. In the turbulent regime, the scaling $\beta = 2/7$ is found instead [14]. Recently, a theory developed by Grossmann and Lohse [9, 15, 16] incorporates the heat transfer contributed by both the thermal boundary layers and the bulk mixing, and is found to be consistent with experimental measurements and numerical simulations.

In this limit of high Ra, a large-scale circulation (LSC) can spontaneously develop, whereby the upwelling and downwelling motions combine to form a circulatory flow with overall direction determined by myriad factors such as domain geometry, external forces (e.g. Coriolis), random perturbations, etc. Under certain conditions, the LSC can change its orientation through either a reversal of the circulation direction [17] or a slow migration of the orientation [18]. The development and reversal of LSC have been observed in controlled laboratory experiments [14, 19–27] and numerical simulations [24, 28], leading to many theories exploring its origin and control [17, 22, 29, 30].

[31] used direct numerical simulations (DNS) to examine LSC dynamics in the annular domain shown in Fig. 1(a). The fluid fills the annulus and is heated from below via a linear temperature profile imposed along the outer ring. As

* nickmoore83@gmail.com
† machuang@nyu.edu

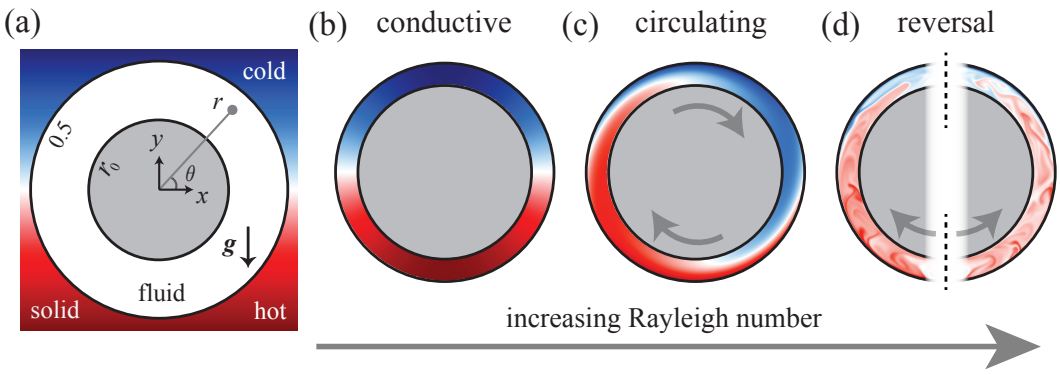

FIG. 1. Thermal convection in an annular domain. (a) The 2-dimensional annular fluid domain $r \in [r_0, \frac{1}{2}]$ is embedded in a solid background with constant vertical temperature gradient. (b) At low Ra, the fluid is motionless and the heat only conducts. (c) Increasing Ra beyond critical, the fluid circulates unidirectionally. (d) Further increasing Ra leads to the reversals of LSC. In (b)-(d), $\mathrm{Pr} = 4$ and $r_0 = 0.4$, and the Rayleigh numbers are (b) $\mathrm{Ra} = 1.4 \times 10^5$, (c) $\mathrm{Ra} = 2.2 \times 10^6$, and (d) $\mathrm{Ra} = 1.6 \times 10^9$. Movies of (b)-(d) are included as Supplemental Material.

Ra increases, a sequence of dynamical states emerge, including a state of pure conduction [Fig. 1(b)], a state of steady circulation in either the clockwise or counterclockwise direction [Fig. 1(c)], and a state in which the LSC reverses direction spontaneously [Fig. 1(d)]. Numerical simulations of these states are included in Supplemental Material. By exploiting simplifications made possible by the annular geometry, [31] systematically derived a low-dimensional ODE model from the governing Navier-Stokes Boussinesq equations that successfully recovers the range of dynamical states with quantitative accuracy.

While the LSC dynamics have been carefully characterized, the heat transfer properties associated with the annular geometry have received less attention. Interestingly, the nature of heat transfer in an annulus may fundamentally differ from the case of classical Rayleigh-Bénard convection (RBC). In RBC, three mechanisms contribute significantly to heat transfer: thermal boundary layers, circulatory motion, and bulk motion through the center of the domain. In the annulus, however, the inner boundary acts as an obstacle that severely impedes motion through the center. In this way, the annular geometry mitigates the effect of bulk motion, so that circulatory and boundary-layer effects can be examined in isolation. How does Nu scale with Ra in this geometry? Can we derive a model that accurately captures the heat transfer mechanism there? We answer these questions by reducing the Navier-Stokes-Boussinesq equations to a set of low-dimensional PDEs, whose solutions recover the boundary layer structure of the full equations and agree with results obtained from full DNS.

In what follows, we will outline the equations and DNS method in Sec. II, summarize the DNS results and the previous ODE model in Sec. III, and derive the PDE model and show how its results match the DNS in Sec. IV. Finally, we will summarize the present results and discuss future directions in Sec. V.

II. EQUATIONS AND DNS METHOD

The dimensionless Navier-Stokes-Boussinesq equations for velocity $\boldsymbol{u}$, pressure p, and temperature T are

$$\frac{\partial \boldsymbol{u}}{\partial t} + \boldsymbol{u} \cdot \nabla \boldsymbol{u} = -\nabla p + \mathrm{Pr} \nabla^2 \boldsymbol{u} + \mathrm{Pr}\,\mathrm{Ra}\, T \boldsymbol{e_y}, \tag{1}$$

$$\frac{\partial T}{\partial t} + \boldsymbol{u} \cdot \nabla T = \nabla^2 T, \tag{2}$$

$$\nabla \cdot \boldsymbol{u} = 0. \tag{3}$$

Here, we have rescaled length by the domain height h, time by the diffusive time scale h^2/κ (κ is the thermal diffusivity), and temperature by difference ΔT between the top and bottom temperatures imposed on the outer ring. After rescaling, the annular domain of fluid is bounded between radius r_0 and $r_1 = 1/2$ as shown in Fig. 1(a), and the temperature lies in the range $T \in [0, 1]$. Three dimensionless numbers arise: the Rayleigh number $\mathrm{Ra} = (\beta_T \Delta T h^3 g)/(\nu\kappa)$, the Prandtl number $\mathrm{Pr} = \nu/\kappa$, and the domain aspect ratio $r_0 = R_0/h$, where β_T is the thermal expansion coefficient, g is the acceleration due to gravity, ν is the kinematic viscosity, and R_0 is the dimensional radius of the inner boundary.

In polar coordinates, $\boldsymbol{u} = u\boldsymbol{e}_\theta + v\boldsymbol{e}_r$ where $\boldsymbol{e}_r$ and $\boldsymbol{e}_\theta$ are the unit vectors in the r and θ directions, the boundary conditions become

$$u = v = 0 \qquad \text{at } r = r_0 \text{ and } r = 1/2, \tag{4}$$

$$\frac{\partial T}{\partial r} = 0 \qquad \text{at } r = r_0, \tag{5}$$

$$T = \frac{1 - \sin\theta}{2} \quad \text{at } r = 1/2. \tag{6}$$

We use a pseudo-spectral Chebyshev-Fourier method with implicit-explicit time stepping to solve Eqs. (1) to (3) with boundary conditions Eqs. (4) to (6). In particular, the method recasts Eqs. (1) to (3) in streamfunction-vorticity form [32–34]. The details of our numerical implementation can be found in [31], where second-order convergence in time and spectral accuracy in space were verified.

Without fluid motion ($\boldsymbol{u} = \boldsymbol{0}$), it is easy to solve Eq. (2) and obtain the temperature distribution of the conductive state, $T_{\text{cond}} = 1/2 - (r + r_0^2/r)\sin\theta/(1 + 4r_0^2)$. With fluid motion, we can define two dimensionless numbers: the Nusselt number measuring the heat transfer rate and the Reynolds number reflecting the flow rate,

$$\text{Nu} = \frac{\langle \int_0^\pi (\partial_r T)|_{r=1/2}\, d\theta \rangle}{\int_0^\pi (\partial_r T_{\text{cond}})|_{r=1/2}\, d\theta}, \quad \text{Re} = \text{Pr}^{-1}\langle \max|\boldsymbol{u}| \rangle, \tag{7}$$

where $\langle\cdot\rangle$ is the long-time average operation.

We introduce three coarse-grained variables to describe the heat and flow structures that emerge during annular convection, namely the fluid center of mass (CoM) (X, Y) and the fluid angular momentum L. The angular momentum describes, to leading order, the overall circulatory motion that arises, while (X, Y) quantifies how buoyancy variations alter the CoM. For example, heating the annulus from below, with no flow response, raises the CoM above the annulus center, $Y > 0$, whereas circulatory motion may offset the CoM horizontally. These variables are defined by,

$$X = -\frac{1}{\text{A}_0}\int_\Omega r\, T\cos\theta\, dA\,, \quad Y = -\frac{1}{\text{A}_0}\int_\Omega r\, T\sin\theta\, dA\,, \quad L = \frac{1}{\text{A}_0}\int_\Omega ru\, dA, \tag{8}$$

where $\text{A}_0 = \pi(1 - 4r_0^2)/4$ is the area of the annulus Ω and $dA = r\, dr d\theta$ is the area element.

III. AN ODE MODEL RECOVERING THE LSC DYNAMICS

[31] derived an ODE system from the Navier-Stokes-Bousinesq equations that describes the evolution of the coarse-grained variables X, Y, and L. Here, we briefly sketch the derivation of the ODE system in a way that will generalize to the new PDE model.

To begin, we expand each of the temperature T and the flow velocity $\boldsymbol{u} = u\boldsymbol{e}_\theta + v\boldsymbol{e}_r$ fields as a Fourier series in θ,

$$T(r, \theta, t) = a_0(r, t) + \sum_{n=1}^{\infty} a_n(r, t)\cos n\theta + b_n(r, t)\sin n\theta, \tag{9}$$

$$u(r, \theta, t) = \sum_{n=-\infty}^{\infty} u_n(r, t)e^{in\theta}, \quad v(r, \theta, t) = \sum_{n=-\infty}^{\infty} v_n(r, t)e^{in\theta}. \tag{10}$$

In the thin channel limit $r_0 \to 1/2$, the dominant balance of incompressibility Eq. (3) implies $v \to 0$ and $\partial_\theta u \to 0$, giving $u = u_0(r, t)$ and $v = 0$ at leading order. Making these substitutions and integrating the u component of Navier-Stokes Eq. (1) over θ gives

$$r^2\frac{\partial u_0}{\partial t} = \frac{r^2}{2}\text{Pr}\cdot\text{Ra}\cdot a_1 + \text{Pr}\left[-u_0 + r\frac{\partial}{\partial r}\left(r\frac{\partial u_0}{\partial r}\right)\right]. \tag{11}$$

Meanwhile, inserting the truncation $u = u_0(r, t)$ into Eq. (2) decouples the temperature modes,

$$r^2\dot{a}_n = -nr\, u_0(r, t)\, b_n - n^2 a_n + r\partial_r\left(r\partial_r a_n\right), \tag{12}$$

$$r^2\dot{b}_n = +nr\, u_0(r, t)\, a_n - n^2 b_n + r\partial_r\left(r\partial_r b_n\right). \tag{13}$$

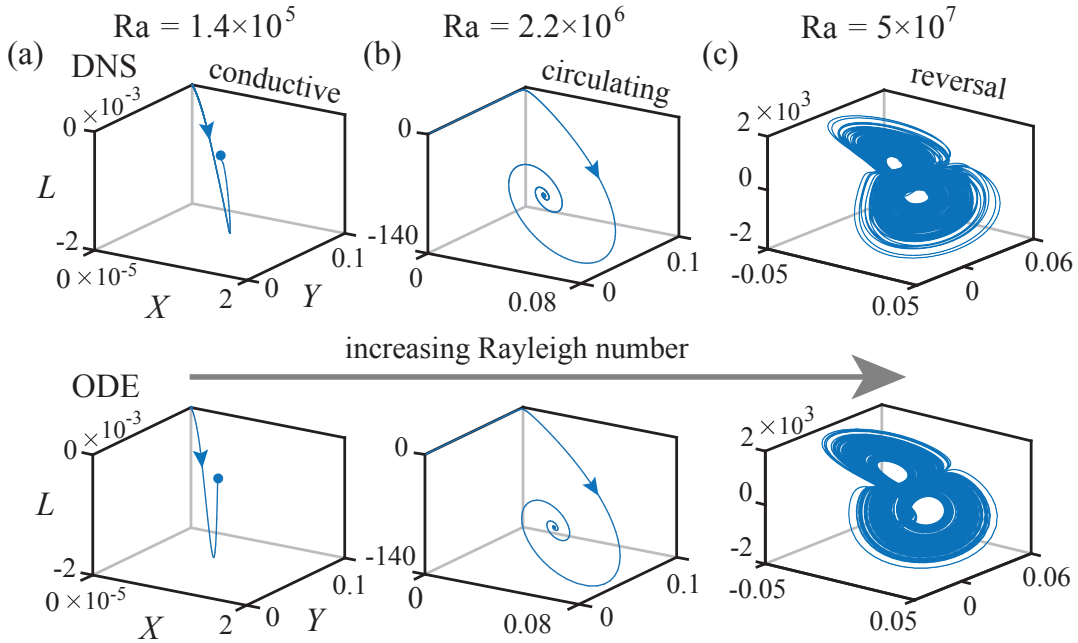

FIG. 2. Trajectories of (L, X, Y) obtained from the DNS result and the ODE model. (a) Conductive state at $\mathrm{Ra} = 1.4 \times 10^5$. (b) Circulating state at $\mathrm{Ra} = 2.2 \times 10^6$. (c) Reversal state at $\mathrm{Ra} = 5 \times 10^7$. In all simulations, $\mathrm{Pr} = 4$ and $r_0 = 0.4$.

The boundary conditions for Eqs. (11) to (13) are

$$u_0 = \partial_r a_n = \partial_r b_n = 0 \qquad \text{at } r = r_0, \tag{14}$$

$$u_0 = 0,\ a_0 = 1/2,\ b_1 = -1/2, \text{ all others vanish} \qquad \text{at } r = r_1. \tag{15}$$

for $n = 0, 1, 2, \cdots$.

By representing u_0, a_1, and b_1 each as a truncated Laurent series in r and inserting into Eqs. (11) to (13), [31] obtained the following dynamical system for the evolution of (L, X, Y):

$$\dot{L} = -\mathrm{Ra}\,\mathrm{Pr}\,X - \alpha \mathrm{Pr}\,L, \tag{16}$$

$$\dot{X} = -kLY + \gamma L - \beta X, \tag{17}$$

$$\dot{Y} = +kLX + \delta - \beta Y, \tag{18}$$

where $\alpha, \beta, \delta, \gamma, k$ are positive constants.

Linear stability analysis of Eqs. (16) to (18) reveals two critical Rayleigh numbers [31]: Ra_1^* marks the loss of stability of the conductive state (Fig. 1(b)) and the simultaneous emergence of the (bistable) circulating states (Fig. 1(c)), while Ra_2^* marks the loss of stability of the circulating state and the subsequent onset of LSC reversals (Fig. 1(d)). As Ra increases, Fig. 2 shows trajectories of $(L(t), X(t), Y(t))$ obtained from DNS (top) and the ODE system (bottom), both exhibiting the same state transition that was shown in Fig. 1. In Fig. 2, the initial conditions are the same for the DNS and ODE, and $\mathrm{Pr} = 4$ and $r_0 = 0.4$ are set for all simulations, yielding $\mathrm{Ra}_1^* = 7.3 \times 10^5$ and $\mathrm{Ra}_2^* = 1.6 \times 10^7$. In Fig. 2(a), $\mathrm{Ra} < \mathrm{Ra}_1^*$ so the fluid is motionless and the heat conducts through; In Fig. 2(b), $\mathrm{Ra}_1^* < \mathrm{Ra} < \mathrm{Ra}_2^*$ and the flow circulates unidirectionally, converging to a steady circulating state; In Fig. 2(c), $\mathrm{Ra}_2^* < \mathrm{Ra}$, LSC reversal is possible and the dynamics are chaotic.

For the parameters selected in Fig. 2, the ODE system Eqs. (16) to (18) recovers LSC dynamics with surprising detail. To evaluate the accuracy of the model over a wider range of parameters, we next focus on the coarse-grained variables Nu and Re, defined in Eq. (7), along with the root-mean-square average of L, which reflects the overall strength of the LSC. These quantities can be directly obtained from the ODE solutions as

$$L_{\mathrm{rms}} = \sqrt{\langle L^2 \rangle}, \quad \mathrm{Re} = \frac{12(1 - \sqrt{2r_0})}{\mathrm{Pr}(1 + \sqrt{2r_0})} L_{\mathrm{rms}}, \tag{19}$$

$$\mathrm{Nu} = \frac{48(1 + 2r_0)(1 + 4r_0^2)}{(1 - 2r_0)^2(1 + 6r_0 + 16r_0^2)} \left[\frac{1 + 2r_0 + 4r_0^2}{12(1 + 2r_0)} - \langle Y \rangle \right]. \tag{20}$$

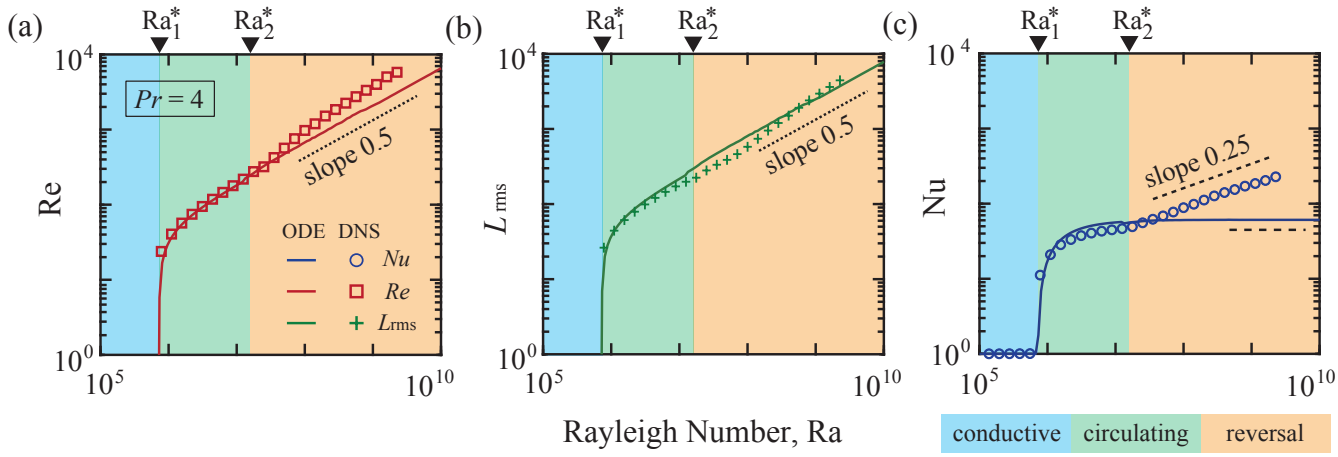

FIG. 3. Re, $L_{\rm rms}$, Nu measured from the DNS and the ODE model. Reynolds number (a) and fluid angular momentum (b) are zero when $\mathrm{Ra} < \mathrm{Ra}_1^*$ but have a 0.5 power-law scaling at high Ra. Both the DNS (symbols) and the ODE (curves) solutions capture this scaling. (c) Nusselt number is unity for the conductive state $\mathrm{Ra} < \mathrm{Ra}_1^*$ and has a 0.25 power-law scaling for high Ra. In this limit, the ODE model approaches a constant Nu, thus it fails to capture the heat transfer of annular convection. In all simulations, $\mathrm{Pr} = 4$ and $r_0 = 0.4$, and two critical Rayleigh numbers are identified as $\mathrm{Ra}_1^* = 7.3 \times 10^5$ and $\mathrm{Ra}_2^* = 1.6 \times 10^7$.

Here, Nu is computed by its definition Eq. (7) with the truncated temperature field $T = a_1(r,t)\cos\theta + b_1(r,t)\sin\theta$, and $\langle Y \rangle$ is the mean height of the fluid CoM. Physically, higher value of $\langle Y \rangle$ means the cold fluid stays higher in space, thereby lowering the heat flux leaving the top boundary.

In Fig. 3, Re, $L_{\rm rms}$, and Nu are plotted for both the DNS (symbols) and ODE (curves). The Reynolds number and LSC strength in Fig. 3(a)-(b) show good agreement between the ODE and the DNS: For $\mathrm{Ra} < \mathrm{Ra}_1^*$, there is no fluid motion so both Re and $L_{\rm rms}$ vanish; For high Ra, a common power law with exponent 0.5 exists as Eq. (19) indicates that Re and $L_{\rm rms}$ are proportional to each other. The scaling $\mathrm{Re} \sim \mathrm{Ra}^{0.5}$ is also present in the classic RBC [9], and we will later verify this scaling through a dominant-balance analysis.

Figure 3(c) shows the heat transfer rate as quantified by the Nusselt number, Nu. Below the threshold $\mathrm{Ra} < \mathrm{Ra}_1^*$, Nu is identically one as heat transfer is purely conductive. For $\mathrm{Ra} > \mathrm{Ra}_1^*$, Nu increases with Ra as convective motion sets in and then grows in strength. The ODE model predicts the Nu-Ra behavior reasonably well in the range $\mathrm{Ra}_1^* < \mathrm{Ra} < \mathrm{Ra}_2^*$, but for $\mathrm{Ra} > \mathrm{Ra}_2^*$ there is considerable discrepancy. The DNS shows that Nu continues to grow as Ra increases, with the measured data points suggesting the power law $\mathrm{Nu} \sim \mathrm{Ra}^{0.25}$. The ODE model, however, predicts Nu to approach an asymptote. In fact, the analysis of [31] shows that the ODE-model prediction for the CoM height, $\langle Y \rangle$, becomes independent of Ra for large Ra, which through Eq. (20) implies the Nu asymptote seen in Fig. 3(c). The discrepancy in the Nu behavior at large Ra suggests that the ODE model may have oversimplified the temperature field, so its gradient is not correctly captured in the thermal boundary layer. To address this deficiency, we next present a PDE model that accurately resolves the boundary layer structure of annular convection.

IV. PDE MODEL AND BOUNDARY LAYER ANALYSIS

Instead of expanding each of $u_0(r,t)$, $a_1(r,t)$, $b_1(r,t)$ in a Laurent series, we observe that Eqs. (11) to (13) form a closed PDE system:

$$\frac{\partial u_0}{\partial t} = \frac{1}{2}\mathrm{Pr}\cdot\mathrm{Ra}\cdot a_1 + \frac{\mathrm{Pr}}{r^2}\left[-u_0 + r\frac{\partial}{\partial r}\left(r\frac{\partial u_0}{\partial r}\right)\right]. \tag{21}$$

$$\frac{\partial a_1}{\partial t} = -\frac{u_0 b_1}{r} + \frac{1}{r^2}\left[-a_1 + r\frac{\partial}{\partial r}\left(r\frac{\partial a_1}{\partial r}\right)\right], \tag{22}$$

$$\frac{\partial b_1}{\partial t} = +\frac{u_0 a_1}{r} + \frac{1}{r^2}\left[-b_1 + r\frac{\partial}{\partial r}\left(r\frac{\partial b_1}{\partial r}\right)\right], \tag{23}$$

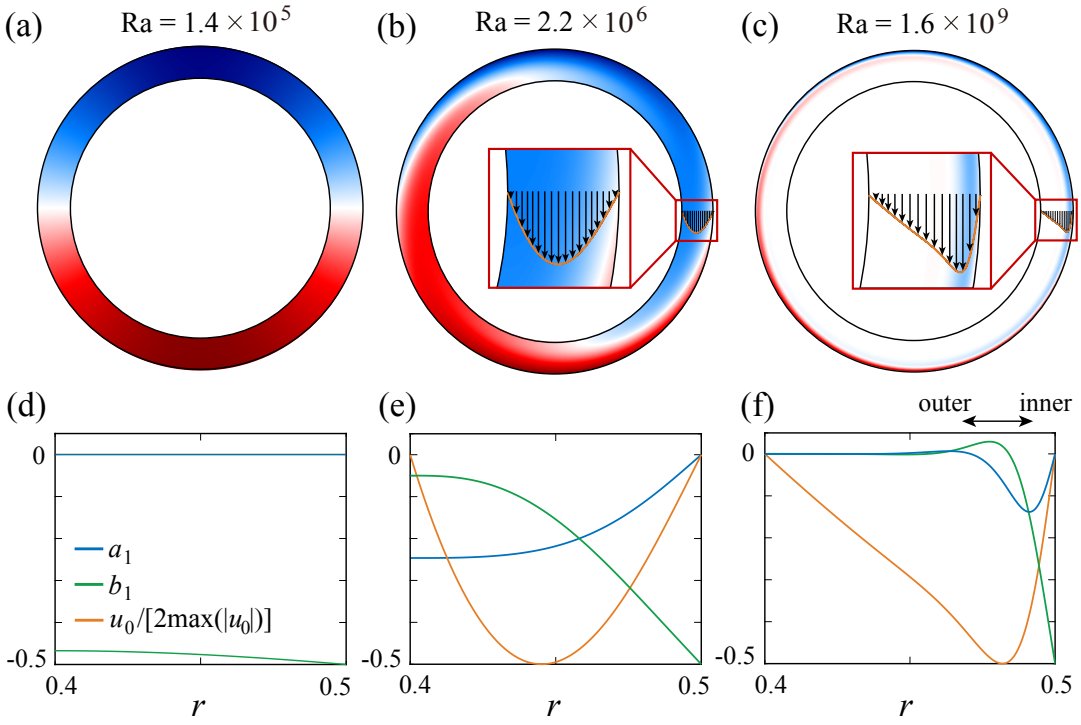

FIG. 4. Steady-state PDE solutions of the flow and temperature fields. (a)-(c) show the PDE solutions with increasing Ra. Thermal and momentum boundary layers develop at high Ra as shown in the zoom-in view (inset) of (c). (d)-(f) show the distribution of a_1, b_1, and u_0 corresponding to (a)-(c). In all simulations, $\mathrm{Pr} = 4$ and $r_0 = 0.4$.

with Eqs. (14) and (15) giving boundary conditions,

$$u_0 = 0, \quad \partial_r a_1 = 0, \quad \partial_r b_1 = 0 \qquad \text{at } r = r_0, \tag{24}$$

$$u_0 = 0, \quad a_1 = 0, \quad b_1 = -1/2 \qquad \text{at } r = r_1. \tag{25}$$

Equations (21) to (25) can be interpreted as a *reaction-diffusion* system, and it can be solved by standard numerical methods [32, 35]. Here, we use a pseudo-spectral Chebyshev-Fourier method to discretize u_0, a_1, b_1 in space and an implicit-explicit method to step forward in time [31]. In particular, our numerical solutions suggest that Eqs. (21) to (25) approaches a steady-state for all Ra and Pr tested. Hereafter, our main focus is the steady-state solutions $a_1 = a_1(r)$, $b_1 = b_1(r)$, and $u_0 = u_0(r)$.

Figure 4 shows the steady solutions of Eqs. (21) to (23) at 3 different Rayleigh numbers. In Fig. 4(a)-(c), the temperature field is recovered by evaluating $T = 1/2 + a_1(r)\cos\theta + b_1(r)\sin\theta$, and the flow profile $u = u_0(r)$ is shown in the insets. The distribution of a_1, b_1, and u_0 is shown in Fig. 4(d)-(f).

For Fig. 4(a) and (d), $\mathrm{Ra} < \mathrm{Ra}_1^*$ so there is no fluid motion. An exact solution $a_1 = u_0 = 0$ and $b_1(r) = -(4r + r_0^2)/(4 + 16r_0^2)$ exists which recovers the conductive temperature distribution T_{cond} in Eq. (7). Increasing $\mathrm{Ra} > \mathrm{Ra}_1^*$, the circulating state emerges and it is shown in Fig. 4(b) and (e). The flow speed $u_0(r)$ is no longer 0 in this case, and the distribution of a_1 and b_1 is modified by the advection of this flow field.

Further increasing Ra, Fig. 4(c) and (f) show a boundary layer forms near $r = r_1$, where the flow speed rapidly drops to 0 and the temperature converges to its boundary value. A length scale, the boundary layer thickness δ, thus marks the region near $r = r_1$ where higher-derivatives in Eqs. (21) to (23) dominate, and we call this the inner region. Outside this inner region, the solution of Eqs. (21) to (23) changes slowly and we name this the outer region.

In the outer region, dominant balance indicates that both a_1 and b_1 vanish in the limit of high Ra, and the flow has a profile $u_0 = c_0(r - r_0^2/r)$ where c_0 is a constant. Taking the limit of $r \to r_1$, we have $a_1 \to 0$, $b_1 \to 0$, and $u_0 \to c_0(r_1 - r_0^2/r_1)$ – these limits set the matching conditions for the inner solution.

For the inner region, we stretch the coordinate by defining $R = (r_1 - r)/\delta$, and we denote $A(R) = a_1(r(R))$, $B(R) = b_1(r(R))$, and $U(R) = u_0(r(R))$. The most dominant terms in Eqs. (21) to (23) for small δ are thus

$$\delta^{-2}A'' = UB, \quad \delta^{-2}B'' = -UA, \quad \delta^{-2}U'' = -\frac{1}{2}\mathrm{Ra}A, \tag{26}$$

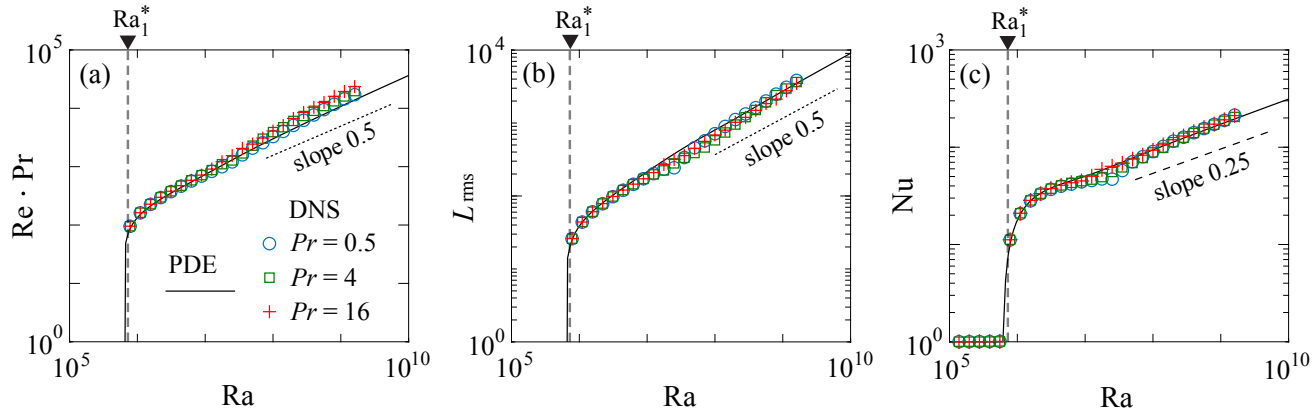

FIG. 5. Re, $L_{\rm rms}$, and Nu obtained from the DNS (symbols) and PDE (curves) solutions. (a) The Reynolds number has a scaling $\mathrm{Re} \propto \mathrm{Pr}^{-1}\mathrm{Ra}^{1/2}$. (b) Fluid angular momentum scales as $L_{\rm rms} \propto \mathrm{Ra}^{1/2}$. (c) Nusselt number has a 1/4 power-law, $\mathrm{Nu} \propto \mathrm{Ra}^{1/4}$. Here $r_0 = 0.4$, leading to $\mathrm{Ra}_1^* = 7.3 \times 10^5$.

together with boundary and matching conditions:

$$U(0) = A(0) = 0,\ B(0) = -1/2;\ A(\infty) = B(\infty) = 0,\ U(\infty) = c_0(r_1 - r_0^2/r_1). \tag{27}$$

At high Ra, we assume $A = \mathcal{O}(\mathrm{Ra}^{\mu})$, $B = \mathcal{O}(\mathrm{Ra}^{\nu})$, $U = \mathcal{O}(\mathrm{Ra}^{\lambda})$, and $\delta = \mathcal{O}(\mathrm{Ra}^{\epsilon})$. Balancing Eq. (26) thus indicates $\mu = \nu$, $\lambda = -2\epsilon$, and $-4\epsilon = 1 + \mu$, so we have 3 equations for 4 exponents. To obtain another equation, we consider the magnitude of $F = A^2 + B^2$, which is the power of the first Fourier mode of the temperature.

From Eq. (26), we have $A''A + B''B = 0$, thus

$$F'' = 2\left[A''A + B''B + (A')^2 + (B')^2\right] = 2\left[(A')^2 + (B')^2\right] > 0. \tag{28}$$

The boundary conditions of A and B also indicate $F(0) = 1/4$ and $F(\infty) = 0$.

The Laplace inequality (28) indicates that F satisfies the maximum principle: $F(R)$ can only attain its maximum at either $R = 0$ or $R = \infty$, thus $F \le F(0) = 1/4$. The proof here is straightforward, as otherwise F would attain its maximum at R^*, so $F'(R^*) = 0$ and $F''(R^*) \le 0$, contradicting Eq. (28).

The range of $F = A^2 + B^2$ is thus $[0, 1/4]$, so A and B are $\mathcal{O}(1)$ and $\mu = \nu = 0$. This enables us to conclude $\lambda = 1/2$ and $\epsilon = -1/4$, leading to the scaling

$$A = \mathcal{O}(1),\ B = \mathcal{O}(1),\ U = \mathcal{O}(\mathrm{Ra}^{1/2}),\ \delta = \mathcal{O}(\mathrm{Ra}^{-1/4}). \tag{29}$$

From Eq. (7), we have $\mathrm{Re} = \mathcal{O}(\mathrm{Pr}^{-1}U)$, $L_{\rm rms} = \mathcal{O}(U)$, $\mathrm{Nu} = \mathcal{O}(\delta^{-1})$, so

$$\mathrm{Re} \propto \mathrm{Pr}^{-1}\mathrm{Ra}^{1/2}, \quad L_{\rm rms} \propto \mathrm{Ra}^{1/2}, \quad \mathrm{Nu} \propto \mathrm{Ra}^{1/4}. \tag{30}$$

These scaling laws can indeed be verified against the DNS data. Figure 5 shows the DNS results (symbols) from solving the full Navier-Stokes-Boussinesq equations, the PDE results (solid curves) from solving the reduced Eqs. (21) to (23), and the scaling Eq. (30). Clearly, the PDE solution recovers the boundary layer structure and the correct Nu–Ra scaling, where a simple 1/4 exponent is revealed.

V. DISCUSSIONS

In this manuscript, we have identified three scaling laws of the annular convection: $\mathrm{Re} \propto \mathrm{Ra}^{1/2}$, $L_{\rm rms} \propto \mathrm{Ra}^{1/2}$, and $\mathrm{Nu} \propto \mathrm{Ra}^{1/4}$. The first two scalings agree with the classic RBC, but the Nu-Ra scaling shows an exponent of 1/4 instead. Through our analysis, we derive a PDE model from the governing Navier-Stokes-Boussinesq equations and identify the heat transfer within thermal boundary layer is most responsible for this scaling. In contrast to the classic RBC, the annular geometry of this study does not have a bulk and the flow structure is dominated by a LSC that connects to the no-slip boundary condition through a boundary layer. In the theory of [15], it is shown that both the boundary layer and the bulk mixing contribute to the heat transfer of RBC, thus leading to a different scaling. Our

study, on the other hand, singles out the heat transfer contributed solely by the boundary layer, enabling us to derive a low-dimensional PDE model that recovers the flow and thermal properties of annular convection.

In the ODE model presented in Sec. III, spontaneous reversals of LSC become possible and persistent once $\mathrm{Ra} > \mathrm{Ra}_2^*$. However such reversals do not present in the long-term dynamics of Eqs. (21) to (23), where a steady state exists for arbitrarily high Ra. This steady state captures the Nu-Ra scaling but it precludes the possibility of LSC reversals, as a steady velocity field can only be associated with a unidirectional LSC. We believe this discrepancy arises from the truncation procedure, where only the lowest nontrivial Fourier modes are retained. Including higher order Fourier modes can better resolve the temperature and flow fields and introduce nonlinearity that associates them, and the dynamics of annular convection can be fully recovered only if all Fourier modes are kept in the analysis – this is the basis of our Fourier spectral DNS method.

The higher-order expansion is also needed for annular convection with small r_0. In this case, the fluid is less constrained so radial component of the flow velocity v cannot be taken as 0. Because fo this, our current PDE model works the best for the thin channel ($r_0 \to 1/2$), and we are working on a higher-order expansion of the governing equations so we can analyze the dynamics of small r_0 convection.

As the fluid becomes less constrained, the role of bulk flow and its mixing can potentially modify the LSC dynamics and the heat transfer. This effect is most visible in the limit of $r_0 \to 0$, where the annular convection becomes a disk convection. The LSC reversals there are less regular and the Nu-Ra scaling is closer to the classic RBC [25, 26]. A model, systematically derived from the Navier-Stokes-Boussinesq equations, is still missing for the disk convection. Extending our model to that geometry is thus another future direction, in which case a Fourier-Taylor expansion could probably reveal the dynamics of LSC reversals and capture the heat transfer.

SUPPLEMENTAL MATERIAL

Supplementary movies are available at `https://math.nyu.edu/~jinzi/research/AnnularConvectionHeatTransfer/`.

[1] R. Salmon, *Lectures on Geophysical Fluid Dynamics* (Oxford University Press, 1998).
[2] J.-Q. Zhong, D. Funfschilling, and G. Ahlers, Enhanced heat transport by turbulent two-phase Rayleigh-Bénard convection, Phys. Rev. Lett. **102**, 124501 (2009).
[3] J. A. Whitehead, Moving heaters as a model of continental drift, Phys. Earth Planet. In. **5**, 199 (1972).
[4] J. Zhang and A. Libchaber, Periodic boundary motion in thermal turbulence, Physical Review Letters **84**, 4361 (2000).
[5] J.-Q. Zhong and J. Zhang, Thermal convection with a freely moving top boundary, Phys. Fluids **17**, 115105 (2005).
[6] J. A. Whitehead and M. D. Behn, The continental drift convection cell, Geophys. Res. Lett. **42**, 4301 (2015).
[7] J. M. Huang, J.-Q. Zhong, J. Zhang, and L. Mertz, Stochastic dynamics of fluid–structure interaction in turbulent thermal convection, J. Fluid Mech. **854** (2018).
[8] T. D. de Wit, V. V. Krasnoselskikh, S. D. Bale, J. W. Bonnell, T. A. Bowen, C. H. K. Chen, C. Froment, K. Goetz, P. R. Harvey, V. K. Jagarlamudi, A. Larosa, R. J. MacDowall, D. M. Malaspina, W. H. Matthaeus, M. Pulupa, M. Velli, and P. L. Whittlesey, Switchbacks in the Near-Sun Magnetic Field: Long Memory and Impact on the Turbulence Cascade, Astrophys. J. Suppl. Ser. **246**, 39 (2020).
[9] G. Ahlers, S. Grossmann, and D. Lohse, Heat transfer and large scale dynamics in turbulent Rayleigh-Bénard convection, Rev. Mod. Phys. **81**, 503 (2009).
[10] J. J. Niemela, L. Skrbek, K. R. Sreenivasan, and R. J. Donnelly, Turbulent convection at very high Rayleigh numbers, Nature **404**, 837 (2000).
[11] D. Funfschilling, E. Brown, A. Nikolaenko, and G. Ahlers, Heat transport by turbulent Rayleigh–Bénard convection in cylindrical samples with aspect ratio one and larger, J. Fluid Mech. **536**, 145 (2005).
[12] C. Priestley, Convection from a large horizontal surface, Australian Journal of Physics **7**, 176 (1954).
[13] C. H. B. Priestley, Turbulent transfer in the lower atmosphere, (No Title) (1959).
[14] B. Castaing, G. Gunaratne, F. Heslot, L. Kadanoff, A. Libchaber, S. Thomae, X.-Z. Wu, S. Zaleski, and G. Zanetti, Scaling of hard thermal turbulence in Rayleigh-Bénard convection, Journal of Fluid Mechanics **204**, 1–30 (1989).
[15] S. Grossmann and D. Lohse, Scaling in thermal convection: a unifying theory, J. Fluid Mech. **407**, 27 (2000).
[16] R. J. A. M. Stevens, E. P. van der Poel, S. Grossmann, and D. Lohse, The unifying theory of scaling in thermal convection: the updated prefactors, J. Fluid Mech. **730**, 295 (2013).
[17] F. F. Araujo, S. Grossmann, and D. Lohse, Wind Reversals in Turbulent Rayleigh-Bénard Convection, Phys. Rev. Lett. **95**, 084502 (2005).
[18] E. Brown, A. Nikolaenko, and G. Ahlers, Reorientation of the large-scale circulation in turbulent Rayleigh-Bénard convection, Phys. Rev. Lett. **95**, 084503 (2005).
[19] H. F. Creveling, J. F. D. Paz, J. Y. Baladi, and R. J. Schoenhals, Stability characteristics of a single-phase free convection loop, J. Fluid Mech. **67**, 65 (1975).

[20] M. Gorman, P. J. Widmann, and K. A. Robbins, Chaotic flow regimes in a convection loop, Phys. Rev. Lett. **52**, 2241 (1984).
[21] M. Gorman, P. J. Widmann, and K. A. Robbins, Nonlinear dynamics of a convection loop: a quantitative comparison of experiment with theory, Physica D **19**, 255 (1986).
[22] E. Brown and G. Ahlers, Large-scale circulation model for turbulent Rayleigh-Bénard convection, Phys. Rev. Lett. **98**, 134501 (2007).
[23] H.-D. Xi and K.-Q. Xia, Cessations and reversals of the large-scale circulation in turbulent thermal convection, Phys. Rev. E **75**, 066307 (2007).
[24] K. Sugiyama, R. Ni, R. J. A. M. Stevens, T. S. Chan, S.-Q. Zhou, H.-D. Xi, C. Sun, S. Grossmann, K.-Q. Xia, and D. Lohse, Flow reversals in thermally driven turbulence, Phys. Rev. Lett. **105**, 034503 (2010).
[25] H. Song, E. Villermaux, and P. Tong, Coherent oscillations of turbulent Rayleigh-Bénard convection in a thin vertical disk, Physical Review Letters **106**, 184504 (2011).
[26] Y. Wang, P.-Y. Lai, H. Song, and P. Tong, Mechanism of large-scale flow reversals in turbulent thermal convection, Sci. Adv. **4**, 7480 (2018).
[27] X. Chen, S.-D. Huang, K.-Q. Xia, and H.-D. Xi, Emergence of substructures inside the large-scale circulation induces transition in flow reversals in turbulent thermal convection, J. Fluid Mech. **877**, R1 (2019).
[28] A. Xu, X. Chen, and H.-D. Xi, Tristable flow states and reversal of the large-scale circulation in two-dimensional circular convection cells, Journal of Fluid Mechanics **910**, A33 (2021).
[29] E. N. Lorenz, Deterministic nonperiodic flow, J. Atmos. Sci. **20**, 130 (1963).
[30] R. Ni, S.-D. Huang, and K.-Q. Xia, Reversals of the large-scale circulation in quasi-2D Rayleigh–Bénard convection, J. Fluid Mech. **778**, R5 (2015).
[31] N. J. Moore and J. M. Huang, Large-scale circulation reversals explained by pendulum correspondence, Journal of Fluid Mechanics **993**, A3 (2024).
[32] R. Peyret, *Spectral methods for incompressible viscous flow*, Vol. 148 (Springer Science & Business Media, 2002).
[33] J. M. Huang, M. J. Shelley, and D. B. Stein, A stable and accurate scheme for solving the Stefan problem coupled with natural convection using the Immersed Boundary Smooth Extension method, J. Comput. Phys. **432**, 110162 (2021).
[34] J. M. Huang and J. Zhang, Rayleigh-Bénard thermal convection perturbed by a horizontal heat flux, J. Fluid Mech. **954**, 10.1017/jfm.2022.1035 (2022).
[35] L. N. Trefethen, *Spectral methods in MATLAB* (SIAM, 2000).